https://doi.org/10.1016/j.ijhydene.2018.01.181

Activation and Failure Mechanism of $La_{0.6}Sr_{0.4}Co_{0.2}Fe_{0.8}O_{3-\delta}$ Air Electrode in Solid Oxide Electrolyzer Cells under High-Current Electrolysis

Zehua Pan[a,b,d*], Qinglin Liu[a], Meng Ni[c], Renzhi Lyu[d], Ping Li[d], Siew Hwa Chan[a,b,*]

a. Energy Research Institute at NTU (ERIAN), Nanyang Technological University, Singapore, 639798, Singapore

b. School of Mechanical and Aerospace Engineering, Nanyang Technological University, Singapore, 639798, Singapore

c. Building Energy Research Group, Department of Building and Real Estate, The Hong Kong Polytechnic University, Hung Hom, Kowloon, Hong Kong

d. Consultancy Service Division, Automotive Data Center, China Automotive Technology & Research Center, Tianjin, China, 300300

*Corresponding authors (zpan001@e.ntu.edu.sg; mshchan@ntu.edu.sg)

Abstract: This work investigates the activation and delamination of $La_{0.6}Sr_{0.4}Co_{0.2}Fe_{0.8}O_{3-\delta}$ (LSCF) air electrode of solid oxide electrolyzer cells sintered on yttria-stabilized zirconia (YSZ) electrolyte. After polarization with an electrolysis current of 1 A cm^{-2} for 24 h at 800 ℃, the LSCF electrode delaminates accompanied by an increase of ohmic and polarization resistance. Notably, polarization resistance decreases at the beginning. By scanning electron microscopy (SEM), a thin but dense layer is observed at the LSCF–YSZ interface of an as-prepared sample, which is identified as $SrZrO_3$ phase by X-ray diffractometry. This layer causes the initial high polarization resistance due to retarded ionic and electronic conductivity. After the test, SEM reveals that the $SrZrO_3$ layer delaminates from YSZ electrolyte. Moreover, energy dispersive X-ray tests confirm that Co diffuses to the $SrZrO_3$ layer and $SrZrO_3$–YSZ interface. Later, the LSCF electrode with Co-containing $SrZrO_3$ layer is shown to perform better than that with pure $SrZrO_3$ layer. Thus, Co diffusion can be the reason for the initial decrease of polarization resistance and renders the generation of oxygen at $SrZrO_3$–YSZ interface during the electrolysis. Owing to its limited porosity, the $SrZrO_3$ layer traps the generated oxygen. High pressure eventually builds up at the $SrZrO_3$–YSZ interface driving the delamination of $SrZrO_3$ layer, and hence the entire LSCF electrode.

Keywords: $La_{0.6}Sr_{0.4}Co_{0.2}Fe_{0.8}O_{3-\delta}$ air electrodes; Co diffusion; Activation of air electrode; Delamination of air electrode; Solid oxide electrolyzer cell

1. Introduction

The solid oxide electrolyzer cell (SOEC) has attracted tremendous attention in recent years as it can produce hydrogen efficiently through high-temperature water electrolysis (HTE) [1-11]. The produced hydrogen can be subsequently used as a fuel for the reverse mode, solid oxide fuel cell (SOFC), to generate electricity. When the energy provided to the water electrolysis in the SOEC comes from renewable energy, the cycle is totally carbon neutral. In addition, many efforts were also made to co-electrolyze water and carbon dioxide in order to obtain syngas electrochemically [12-14]. Recently, direct seawater electrolysis was also found viable [15], indicating the flexible application of this technique.

However, one critical issue associated with SOEC is the delamination of air electrode, especially during high-current electrolysis [16-28]. Several mechanisms accounting for the delamination phenomenon of LSM ($La_{1-x}Sr_xMnO_{3-\delta}$)-based air electrode have been proposed [16-19, 21, 22]. Modeling work done by Virkar [16] showed that high oxygen partial pressure could develop within the electrolyte near the electrolyte–air electrode interface, causing the delamination of electrode. Experimentally, Laguna-Bercero et al. [22] tested a fuel electrode-supported Ni–YSZ|YSZ|LSM–YSZ cell under extreme high voltage up to 2.8 V and found that the oxygen electrode delamination is associated with the high oxygen partial pressure gradient taking place at the electrolyte–air electrode interface.

In addition, inter-diffusion of the atoms between LSM and YSZ was proposed to be able to facilitate oxygen generation and cause delamination. Rashkeev and Glazoff [19] used a combination of first-principles, density-functional-theory calculations and thermodynamic modelling and found that the inter-diffusion of different atoms across the LSM–YSZ interface significantly affected structural stability of the materials and their interface. Particularly, La and

Sr substitutional defects positioned in ZrO_2 oxide and near LSM–YSZ interface significantly changed oxygen transport which might develop pressure build-up in the interfacial region and eventually develop delamination process. Kim et al. [20] have applied electrolysis current of 1.5 A cm^{-2} at 750 °C for 120 h on symmetric cells composed of YSZ electrolytes and LSM–YSZ electrodes. After the test, extensive inter-diffusion between the two phases and intergranular fracture along YSZ grain boundaries were observed. They discussed that the migrated La, Sr and Mn impurities would segregate along the grain boundary of YSZ electrolyte and participate in structural degradation by facilitating generation of oxygen gas.

Apart from the buildup of high oxygen partial pressure, morphological change and phase change of air electrodes were also experimentally observed when delamination happened. Keane et al. [21] found that the high oxygen pressure developed at the electrolyte–electrode interface could aggravate the formation of $La_2Zr_2O_7$ second phase, which led to the detachment of the air electrode. Chen and Jiang [17, 18] observed that nanoparticles appeared at the electrolyte–electrode interface after the electrolysis test. They reported that the high oxygen partial pressure could disintegrate the LSM particles and thus weaken the bonding between the electrolyte and the electrode. Later, based on this mechanism, Zhang et al. [29] proposed a model that can well describe the evolution of the electrochemical performance. In light of the above findings, Li et al. [30] applied Mn modification on the YSZ electrolyte and found that this could mitigate the delamination of the LSM electrode by preventing the $La_2Zr_2O_7$ formation and oxygen accumulation.

Currently, $La_xSr_{1-x}Co_yFe_{1-y}O_{3-\delta}$ (LSCF) is under intensive research as potential air electrode of SOECs to replace traditional LSM-based electrode [24-28, 31-37]. As a mixed ionic and electronic conductor (MIEC) with high catalytic activity, LSCF performs much better than LSM as cathode

in SOFCs [38-41]. Besides, the ionic conductivity of LSCF is believed to be able to extend the reaction sites into the bulk of the air electrode and, in turn, decrease the oxygen partial pressure at the interface [2]. However, the delamination of LSCF electrode has also been reported after 50 h test [24]. Even though gadolinium doped ceria (GDC) was employed as an interlayer, the delamination of the GDC interlayer from the YSZ electrolyte has also been observed [25-28]. Additionally, in spite of the delamination phenomenon, it was previously reported that the initial passing of anodic current had an activation effect on the LSCF electrode [35]. As YSZ is still the first choice as electrolyte material [42-45], the mechanism for the activation and delamination of LSCF electrode based on YSZ electrolyte needs to be fully understood, in order to improve the reliability of LSCF air electrode.

Consequently, this work aims to study the mechanism for the activation and delamination of $La_{0.6}Sr_{0.4}Co_{0.2}Fe_{0.8}O_{3-\delta}$ air electrode based on YSZ electrolyte. Tests were firstly conducted on half-cells to study the electrochemical behavior of the LSCF electrode during high-current electrolysis. Before and after the tests, compositional and morphological changes at the electrode–electrolyte interface were investigated. At last, a mechanism accounting for the electrochemical behavior has been proposed based on the experimental results and observations. In this work, half-cells with LSCF as the working electrode were selected to simplify the testing conditions and to easily build a relationship between the morphological/compositional changes and the performance changes. In the future, the mechanisms proposed in the study will be verified on a full cell.

2. Experimental

In this work, half-cells with three-electrode configuration were used to study the activation and delamination phenomenon of LSCF air electrode. Details of the fabrication procedure has been described previously [35]. Briefly, YSZ powder (8 mol% Y_2O_3-ZrO_2, Tosoh, Japan) was die-

pressed into pellets with 20 mm in diameter and 1 mm in thickness, which were subsequently sintered at 1450 ℃ for 4 h. After that, LSCF ($La_{0.6}Sr_{0.4}Co_{0.2}Fe_{0.8}O_{3-\delta}$, Fuelcellmaterials, US) cathode slurry was applied on one side of the YSZ electrolyte and sintered at 1000 ℃ for 2 h, with an effective area of 0.5 cm^2 (the outer diameter is 8 mm) and a thickness of ~ 15 μm. Another group of half-cells with LSCF electrodes sintered at a much lower temperature of 800 ℃ was also fabricated for comparison. For convenience sake, the half-cells with YSZ electrolytes and LSCF electrodes sintered at 1000 ℃ and 800 ℃ are henceforth referred to as Y1000 and Y800, respectively. Pt was employed to serve as counter and reference electrodes. Finally, another layer of Pt was applied onto the cathode layer as the current collector.

For the electrochemical characterization, a homemade test station as shown in Figure S1 was employed. The sample was held horizontally between two vertical 4-bore alumina tubes with an outer diameter of 6 mm. To improve the contact, a platinum mesh was also placed in between the working electrode and the alumina tube. LSCF air electrode was exposed to ambient air and applied with an electrolysis current of 1 A cm^{-2} to simulate the SOEC operation at 800 ℃. Electrochemical impedance spectra (EIS) were recorded by a Solartron 1255B frequency response analyzer (FRA) under open circuit voltage (OCV). After the removal of the electrolysis current, the cell was kept under OCV for 60 s before the start of the EIS test each time. The frequency ranges from 100 kHz to 0.1 Hz with AC amplitude of 10 mV.

To observe the changes at the interface between the LSCF electrode and the YSZ electrolyte before and after the test, the surface of YSZ electrolyte in contact with LSCF electrode was examined. The LSCF electrodes were removed by soaking the half-cells in diluted nitric acid (10 wt. %) under ultrasonic for 30 min. Field emission scanning electron microscope (FESEM, JSM-7600F, JEOL, Japan) coupled with energy dispersive X-ray (EDX) detector was adopted to check

the morphological and compositional changes. X-ray diffractometer (XRD, Empyrean, PANalytical) with a radiation source of Cu Kα was used to detect the products arising from possible interfacial reactions and the change of the possible second phase after the polarization test by examining the above-obtained YSZ surfaces.

3. Results and discussion

3.1 Electrochemical response evolution of half-cells

Figure 1 shows the electrochemical behaviors of different half-cells during the electrolysis test with an electrolysis current of 1 A cm^{-2} at 800 ℃ for 24 h. Figure 1a is the Nyquist plot evolution of Y1000. In a Nyquist plot, the high-frequency intercept of the impedance arc with the real axis represents the ohmic resistance, R_S, while the difference between the high- and low-frequency intercepts denotes the polarization resistance, R_P, of the electrode. The changes of R_P and R_S, as well as the change of the voltage for Y1000, were extracted and drawn in Figure 1b. The evolution of the voltage and the resistances shows a pattern that can be resolved into three distinctive regions as indicated in the figure. At the beginning, the R_P and R_S are 1.53 and 1.66 Ω cm^2, respectively. In region I, a substantial activation took place within 30 min, during which R_P decreases from 1.53 to 0.59 Ω cm^2. R_S also presents a slight decrease from 1.66 to 1.52 Ω cm^2. This initial activation behavior is in consistence with previous observation on LSCF air electrode and the authors speculated that this could be associated with the incorporation of surface Sr [35].

After the initial activation period, R_S becomes relatively stable, increasing slightly from 1.52 to 1.56 Ω cm^2 in region II. At the same time, R_P decreases from 0.59 to 0.29 Ω cm^2 in 17.5 h, demonstrating a slower decreasing rate compared with that in region I. Subsequently, in region III, R_S increases notably from 1.56 to 2.01 Ω cm^2 within 6 h and R_P increases to 0.32 Ω cm^2. After the test, the LSCF electrode delaminated from the YSZ electrolyte as shown in the cross-section SEM

image in Figure S2a. It should be noted that in our test station, the sample is held between two 4-bore alumina tubes. Thus, although the electrode delaminated, it was still pressed onto the YSZ electrolyte by the upper alumina tube, enabling EIS tests. The delamination phenomenon is in accordance with the increase of R_S and R_P as the contact between the LSCF electrode and the YSZ electrolyte was weakened. Moreover, it is interesting to note that an activation process presents at the beginning of the test on R_P. More discussion will be made later.

For comparison purpose, a Y800 underwent the same electrolysis test for 24 h and the results are shown in Figure 1d and 1e. As can be seen in Figure 1d, the initial R_P and R_S of Y800 are 0.14 and 1.87 Ω cm^2, respectively. The initial R_P of Y800 is substantially smaller than that of Y1000, due to the lowered sintering temperature, in agreement with previous reports [35, 46]. The electrochemical behavior of Y800 during the test was also divided into three regions in the same way as Y1000 was. Two differences can be identified between Y1000 and Y800 in the electrochemical behavior. Firstly, no significant activation process happens on R_P of Y800. Secondly, at the end of test, R_S of Y1000 increased abruptly while R_S of Y800 did not and ended up at 1.82 Ω cm^2. After unloading Y800, one can see no electrode delamination of Y800 as shown in Figure S2b, in accordance with the more stable R_S. This also indicates that the delamination did not happen during the cooling and unloading process.

To study the activation process of LSCF electrode in more details, distribution function of relaxation times (DRTs) [47] were calculated and the results are presented in Figure 1c and 1f for Y1000 and Y800, respectively, for the first 2 h of the electrolysis test. In Figure 1f, the DRT analysis of Y800 at the beginning of the electrolysis test shows a main peak at 6×10^2 Hz (denoted as medium-frequency arc in the figure, M) and another two small peaks at 30 Hz (denoted as low-frequency arc in the figure, L) and 2 Hz. In comparison, the DRT analysis of Y1000 shows three

peaks at 2 Hz, 10 Hz and 2×10^2 Hz (denoted as low-frequency arc in the figure, L) and an additional high-frequency arc at 2×10^3 Hz (denoted as high-frequency arc in the figure, H). According to previous reports [47-50], the process at a frequency around 10^3 Hz is related to charge transfer (electron and oxygen ion transfer) process, the process with a frequency around 10^2 Hz represents the mass transfer (oxygen adsorption/desorption, dissociation/association and diffusion) process and the process around 10 Hz is associated with gas diffusion.

From Figure 1c one can see that after the first 30 min of the electrolysis test of Y1000, low-frequency peak shrinks and high-frequency arc disappears with the emergence of a medium-frequency peak. After that, low-frequency peak increases again and gradually medium-frequency peak diminishes and merges into the low-frequency peak. For Y800 in Figure 1f, during the initial 30 min test, medium-frequency peak shrinks to a less extent compared with Y1000. After that, another low-frequency peak, L', emerges, which corresponds to the degradation afterwards as shown in Figure 1e. The mechanism of this degradation is unclear at this moment and will be carefully studied in the near future.

In addition, evolution of activation energy of the processes at different frequencies was calculated to gain an insight of the activation phenomenon of Y1000. Due to the fact that the EIS curves tested at 800 ℃ after a period of electrolysis test suffer from severe distortion especially at low-frequency end, which will cause inaccuracies during curve fitting, these curves were excluded. This could be a result of the recovery of the LSCF electrode to its original state from the changes caused by the electrolysis current. Firstly, DRT analysis was conducted to obtain peak information as shown in Figure S3. It can be observed that Y1000 presents three peaks when the testing temperature is equal to or below 750 ℃ while for the rest samples, only medium- and low-frequency arcs can be observed. To make the comparison straightforward, the high- and low-

frequency processes in Y1000 were fitted by only one arc and denoted as medium-frequency arc. Thus, the equivalent circuit used in this work is $LR_S(Q_MR_{P,M})(Q_LR_{P,L})$, where L is inductance, R_S is the ohmic resistance, Q_M and Q_L are the constant phase elements (CPE) for medium- and low-frequencies, $R_{P,M}$ and $R_{P,L}$ are the electrode polarization resistances of medium- and low-frequencies, respectively. Figure S4 shows sample fittings of Y1000 at different temperatures at the beginning of the test and all the fitting parameters can be found in Table S1.

Activation energy of medium-frequency arc, low-frequency arc and the whole arc of Y1000 was calculated based on the fitting parameters and plotted against testing duration in Figure 2. During the initial 2 h electrolysis test, the activation energy of the whole impedance arc decreases. In details, the activation energy of medium-frequency arc increases and the activation energy of the low-frequency arc decreases. The change of activation energy suggests that changes of materials properties have taken place during the electrolysis test. In another word, the activation of LSCF electrode of Y1000 is caused by the change of materials properties.

3.2 Characterization of the electrode-electrolyte interface

The characterization of the electrode–electrolyte interface was conducted by examining the surface of the YSZ electrolyte where it was in contact with the LSCF electrode. The LSCF electrodes were removed using diluted nitric acid except for Y1000 after the test, of which the YSZ electrolyte was observed directly since the LSCF electrode has entirely delaminated.

Figure 3 shows the FESEM images of the cross-section of Y1000 and YSZ electrolyte surfaces before the polarization test. EDX examinations were conducted on the areas indicated in the images and the results are shown in the insets as well as listed in Table 1. Figure 3a is the cross-section of Y1000. As indicated by the red rectangle, a thin layer of ~100 nm in thickness can be observed in between the LSCF electrode and the YSZ electrolyte. In Figure 3b, the electrolyte

surface of Y1000 after the removal of the LSCF electrode is shown. Figure 3d shows a bare surface of the YSZ electrolyte as a comparison, which is clear and the YSZ grains are distinctly visible. In contrast, the surface microstructure of the YSZ electrolyte in Figure 3b is quite different and no grains can be recognized. The YSZ surface of Y800 is shown in Figure 3c, which is similar to bare YSZ electrolyte surface and YSZ grains are clearly observable.

EDX analysis on Y1000 shows that the cations of the surface substance in Figure 3b are Zr (25 at. %) and Sr (12 at. %) with trace La (4 at. %). The other elements in the LSCF phase such as Co and Fe were not detected. Hence, it can be inferred that the observed layer in Figure 3a and the surface in Figure 3b is the inter-diffusion layer between the LSCF electrode and the YSZ electrolyte developed during the sintering process. For Y800, the surface of the electrolyte is composed of Zr (37 at. %) and O (63 at. %), without any other cations from the electrode. Thus, interfacial reaction did not happen on Y800 during the fabrication stage due to the lower sintering temperature.

XRD examinations were conducted to further confirm the phase of the inter-diffusion layer. XRD patterns of the electrolyte surfaces before the test of Y1000 and Y800 are shown in Figure 4a and 4b, respectively. In Figure 4a, the XRD pattern of Y1000 (Corresponding to the surface in Figure 3b) shows the peaks representing $SrZrO_3$ second phase, apart from the peaks corresponding to YSZ phase. One very weak peak of LSCF phase also exists at $2\theta \approx 32.7°$, which is from the residue of the LSCF electrode. In contrast, the XRD pattern of Y800 in Figure 4b shows only a pure YSZ phase without any second phase, consistent with EDX analysis.

Given the above information, it can be confirmed that the inter-diffusion layer shown in Figure 3a and 3b is a layer of $SrZrO_3$ second phase, arising from the high-temperature sintering of the electrode. This agrees with the previous report on the interfacial reaction between LSCF and YSZ

forming insulated $SrZrO_3$ second phase and lowering the electrochemical performance [35]. Furthermore, it should be noted that the $SrZrO_3$ layer is rather dense without any visible holes and it covers the whole surface of the YSZ electrolyte as shown in Figure 3a and 3b. This morphology is quite different from the interface between LSM electrode and YSZ electrolyte, where the formation of convex rings were observed [51]. This demonstrates that the interfacial reaction happened anywhere rather than being restricted to the places where LSCF particles and YSZ electrolyte were in contact, possibly due to the high diffusivity of Sr [52, 53].

After the delamination of the LSCF electrode, YSZ surface of Y1000 was examined by SEM and the images are shown in Figure 5. In Figure 5a, two different morphologies are spotted and indicated by A and B. Figure 5b and 5c show the enlarged images of point A and B, respectively. According to the EDX analysis, the cations at point A are Zr (20 at. %), Sr (16 at. %), La (4 at. %) and Co (3 at. %). Except for Co, the rest cations are identical to those contained in the $SrZrO_3$ layer observed in Figure 3b, suggesting that the substance from point A is the residue of the layer. In comparison, point B is free of any other cations in LSCF except for some Co (5 at. %) and mainly consists of Zr (30 at. %), indicating that this layer is the pure YSZ surface. This observation reveals that the $SrZrO_3$ layer delaminated from the YSZ electrolyte surface during the test rather than that the LSCF electrode delaminated from the $SrZrO_3$ layer. The emergence of Co could come from the diffusion of Co from the LSCF electrode.

XRD examination of the YSZ surface of Y1000 after the test was also conducted and the pattern is shown in Figure 4c, which is similar to that before the test. Peak integration was performed for the YSZ peak at $2\theta \approx 30°$ and the $SrZrO_3$ peak at $2\theta \approx 31°$ to render a semi-quantitative comparison. The results are illustrated in Figure 4. The relative content of $SrZrO_3$ to YSZ fell from 10% before the test to 4% after the test, which corresponds to the residues shown in Figure 5b. This again

proves that the $SrZrO_3$ layer has delaminated. However, although EDX analysis confirms the existence of Co, no peak corresponding to any simple Co oxides were detected. Thus, it is possible that a solid solution has formed.

To further understand the morphological and compositional changes of the electrode–electrolyte interface, two more samples of Y1000 were tested under an electrolysis current of 1 A cm^{-2} at 800 ℃ for 0.5 h and 12 h, respectively. It was observed that the LSCF electrode was still well adhered to the electrolyte after 0.5 h polarization, while the LSCF electrode delaminated partially after 12 h polarization. The electrolyte surfaces of these two samples are shown in Figure 6 (Figure 6b and 6c). For the sample after 0.5 h test, the LSCF electrode was removed by acid washing and for the sample after 12 h test, the part of the electrolyte where the LSCF has delaminated was observed. The electrolyte surfaces of freshly prepared sample (Figure 6a) and the samples tested for 24 h (Figure 6d) are shown together for easy comparison. EDX examinations were also performed on different parts of the surfaces as marked in Figure 6 by capital letters and rectangles and the results are summarized in Table 1.

Comparing Figure 6a and 6b, one can see that after 0.5 h electrolysis test, the surface of the $SrZrO_3$ layer of Y1000 is roughened and the grains of $SrZrO_3$ phase are distinguishable. Besides the morphological changes, the composition has also changed. By EDX, additional 2 at. % Co was detected on area D compared with the sample before the test. Moreover, some stick-like residues can be observed at the grain boundaries as indicated with symbols, C1 to C4, in Figure 6b. EDX analysis shows higher Co content, average 8 at. %, at these places. This finding demonstrates that Co diffusion from the LSCF electrode to the $SrZrO_3$ layer has already happened after the first 0.5 h polarization test. Correspondingly, fast activation was observed as shown in region I in Figure 1b.

In Figure 6c, the YSZ surface of Y1000 after 12 h electrolysis test is found being partially covered with small particles with an average diameter of ~ 60 nm. EDX area analysis (G) shows that Co content is 5 at. %, together with 28 at. % Zr. EDX point-analysis reveals that average Co content is 10 at. % on the particles (E1 to E4), higher than 3 at. % on the places without particles (F1 to F4). Thus, the particles on the YSZ surface is possibly composed of Co-based substance and originated from Co diffusion. Moreover, a nitric acid washed sample was also examined by EDX and has a composition of 6 at. % Co and 31 at. % Zr. Thus, the surface Co is most likely to be Co in YSZ lattice, which is in accordance with the XRD analysis, as simple Co oxides are easily to dissolve into nitric acid.

In Figure 6d, the YSZ surface of Y1000 after 24 h electrolysis test is fully covered by the small particles with an average diameter of ~ 50 nm. Comparing Figure 6d with 6c, although the Co contents are equal (5 at. %), a spread of Co-based particles can be recognized from some parts of the YSZ surface to the whole surface. To sum up, in region II and III of the high-current electrolysis test shown in Figure 1b, the variation of R_P is accompanied by the Co diffusion to the YSZ surface. Yet at the same time, the delamination process is also proceeding, weakening the contact between the electrode and electrolyte. Thus, the first-decrease-and-then-increase behavior of R_P is most likely a result of the trade-off between the Co diffusion and the delamination.

Mutual diffusion of the LSCF electrode and the adjacent electrolyte during electrolysis test has been observed previously by Laurencin et al. [54]. They detected Co diffusion into the GDC interlayer after electrolysis test under 0.5 A cm^{-2} at 850 ℃ for 1500 h. Also, they cannot detect any Co oxide phase by XRD. This could be the result of either the formation of a solid solution or the particle of Co phase was too small to be detected. By EDX mapping, the authors discussed that the Co should exist as a separate phase rather than merging into the lattice of GDC, as the

distribution of Co did not overlap with Ce. By STEM–EDX, the authors inferred that the Co segregates could be Co–Fe oxides. Nonetheless, the exact composition and existing phase of the diffused Co is still unclear and needs further investigation.

From above electrochemical characterization and materials characterization, the following observations are made:

From electrochemical characterization

(a) At the beginning of the electrochemical test, the R_P of Y1000 is substantially higher than that of Y800.

(b) During the electrolysis test at 800 ℃ under 1 A cm^{-2} for 120 h, R_P of Y1000 demonstrates an activation process initially with changes in activation energy. During the last 6 h, R_S of Y1000 increases abruptly. In contrast, R_P and R_S of Y800 shows steady evolution without fast activation or degradation.

From materials characterization

(a) A thin but dense layer composed of $SrZrO_3$ insulated phase is observed at the LSCF–YSZ interface for freshly prepared Y1000, while the surface of YSZ electrolyte of Y800 is clean.

(b) After the electrolysis test, $SrZrO_3$ layer of Y1000, together with the LSCF electrode, delaminates from YSZ electrolyte. Y800 shows no delamination problem.

(c) Diffusion of Co into $SrZrO_3$ layer and onto YSZ electrolyte is detected in Y1000 during the electrolysis test.

Two correlations can be derived from above findings. Firstly, the high initial R_P of Y1000 is accompanied by the formation of $SrZrO_3$ layer. Secondly, the improvement of the performance of Y1000 by 1 A cm^{-2} electrolysis current took place along with Co diffusion to $SrZrO_3$ layer. However, it is hard to conclude at this moment that the $SrZrO_3$ is the sole reason for the high R_P

and that Co diffusion is the reason for the activation of the Y1000. Thus, in the following sections, experiment was conducted to make clear of the above statements.

3.3 Effect of the formation of $SrZrO_3$ layer on the electrochemical performance

It was observed that a thin but dense $SrZrO_3$ layer formed after sintering LSCF electrode at 1000 ℃ and R_P of Y1000 is significantly higher than that of Y800. However, high sintering temperature would also cause other inherent changes of LSCF electrode like Sr surface segregation and particle size increase [55, 56]. Thus, in this part, a Y1000 was fabricated and tested firstly. After that, the LSCF electrode of the Y1000 was removed and again LSCF electrode was re-applied on the YSZ substrate and sintered at 800 ℃. The inherent changes of LSCF electrodes was excluded by the lowing sintering temperature and the effect of $SrZrO_3$ layer can be concluded by comparing the performance of as-prepared Y1000 and the re-applied LSCF electrode. Figure 7 shows the comparison of R_P against testing temperature of Y1000 and the re-applied LSCF electrode sintered at 800 ℃. The re-applied LSCF electrode only shows a slight improvement at lower testing temperatures, demonstrating that the high R_P of Y1000 is dominated by the formation of $SrZrO_3$ layer.

3.4 Effect of Co diffusion on Y1000 (half-cells sintered at 1000 ℃)

To examine the effect of Co diffusion, a Y1000 was firstly tested at 800 ℃ for 24 h with an electrolysis current of 1 A cm^{-2}, during which Co can diffuse to the YSZ electrolyte. After cooling down, the LSCF electrode was found to have delaminated from the electrolyte, which agrees with the above observations. After that, the surface of the YSZ electrolyte substrate from which the LSCF electrode has delaminated was washed by nitric acid and then re-applied with LSCF slurry

followed by sintering at the same temperature of 1000 ℃. At last, EIS test was performed again on the sample.

The YSZ electrolyte surface after the removal of the re-applied LSCF electrode by acid washing was also characterized as shown in Figure 8a. Firstly, EDX analysis of the surface confirms the existence of 7 at. % Co on the YSZ surface, which is much higher than its stoichiometric value. In contrast, no Co was detected on the newly prepared sample (Figure 3b). Secondly, XRD pattern shown in the inset of Figure 8a confirms the formation of 11% $SrZrO_3$ second phase relative to YSZ phase. This value is higher than the 4% $SrZrO_3$ after the 24 h electrolysis test (Figure 4c), demonstrating that $SrZrO_3$ second phase has again formed during the second sintering process. Therefore, by this way, the Co diffused to the YSZ electrolyte during the previous 24 h electrolysis test was included in the LSCF–YSZ interface after the re-application of LSCF electrode and a Co-containing $SrZrO_3$ layer has formed, which can be used to study the effect of Co diffusion.

Figure 8b shows the evolution of R_P of the newly prepared Y1000 and re-applied LSCF electrode sintered at 1000 ℃. For the first 24 h, the change of R_P of the newly prepared LSCF electrode follows the same first-decrease-and-then-increase trend as in Figure 1b. After that, the re-applied LSCF electrode shows a R_P of 0.99 Ω cm^2, which is much smaller than the initial R_P of the newly prepared LSCF electrode, 2.43 Ω cm^2. Another 24 h electrolysis test was also conducted on the re-applied LSCF electrode. A similar activation step for the re-applied LSCF electrode can be observed but to a less extent compared with the freshly prepared one. Specifically, during the first 1 h of the electrolysis test, R_P decreased from 2.43 to 0.80 Ω cm^2 (Decrease by 67%) for the freshly prepared Y1000, while R_P decreased from 0.99 to 0.62 Ω cm^2 (Decrease by 37%) for re-applied LSCF electrode sintered at 1000 ℃. Above results validate that the existing Co substance in the $SrZrO_3$ layer can improve the electrode performance and diminish the activation effect during the

test on the re-applied LSCF electrode. This indicates that the improvement by the electrolysis current is caused by the Co diffusion. Furthermore, Co diffusion could alter the materials properties, which is in agreement with the changes of activation energy during the electrolysis test as analyzed above.

3.5 Discussion

The reaction between LSCF and YSZ when sintered together at high temperature forming $SrZrO_3$ second phase, together with the precipitation of spinel phase, has been reported previously [35]. $SrZrO_3$ is an insulated phase with total conductivity less than 10^{-3} S cm^{-1} at 800 ℃ and the oxygen ion transference number varying from 0.2 to 1 [57]. In this work, a thin but dense layer of $SrZrO_3$ with a thickness of ~100 nm was observed covering the whole YSZ electrolyte surface, leading to the poor conduction of both oxygen species and electrons. As shown in Figure 7, this layer is the main contribution to the initial much larger R_P for Y1000, 1.53 Ω cm^2, than Y800, 0.14 Ω cm^2 (Figure 1). On the other hand, the activation of R_P during the electrolysis test was recognized, which was accompanied by Co diffusion as confirmed by EDX analysis. In Figure 8b, the inclusion of Co in the $SrZrO_3$ layer was shown to not only have a positive influence on the electrochemical performance of the LSCF electrode, but also reduce the activation effect of the electrolysis current. Furthermore, the Co diffusion into $SrZrO_3$ layer could change the materials properties, in accordance with the evolution of activation energy as shown in Figure 2. Consequently, the decrease of R_P of Y1000 during the electrolysis test could be a result of Co diffusion.

Derived from above findings and analysis, a detailed activation and delamination process of Y1000 is schematically shown in Figure 9. In Figure 9a, a thin but dense layer of $SrZrO_3$ second phase forms at the electrode–electrolyte interface (shown in Figure 3b) of a freshly prepared sample, as a result of the high sintering temperature of 1000 ℃. In Figure 9b, after the first 0.5 h

electrolysis test at 1 A cm^{-2}, Co diffuses to the $SrZrO_3$ layer and the surface of the $SrZrO_3$ layer roughens, increasing the electrochemical activity of the $SrZrO_3$ layer. These lead to a substantial decrease of R_P. After that in Figure 9c, the improved electronic conductivity and catalysis activity of the $SrZrO_3$ layer by Co-diffusion renders the generation of oxygen at the $SrZrO_3$–YSZ interface during the electrolysis test. However, the oxygen molecules generated cannot efficiently diffuse away to the atmosphere, due to the low porosity of the $SrZrO_3$ layer. Thus, the accumulated oxygen gradually weakens the bonding between the $SrZrO_3$ layer and the YSZ electrolyte. In Figure 9d, the $SrZrO_3$ layer has partially delaminated and Co-phase emerges on the YSZ electrolyte (Figure 6c) after 12 h test. Eventually (Figure 9e), high oxygen partial pressure causes the complete delamination at the $SrZrO_3$–YSZ interface except for some local residues of $SrZrO_3$ as shown in Figure 5b, resulting in the increase of R_P and R_S. Besides, the surface of the exposed YSZ electrolyte is fully covered with Co-based substance (Figure 6d). However, the exact composition and phase of the Co-based substance is still unclear, which will be investigated in the future.

Above mechanism is also supported by the test on Y800. Due to the much lower sintering temperature, no detectable $SrZrO_3$ second phase formed during the sintering process. Within the testing period of 24 h, delamination phenomenon was not observed on Y800 as shown in Figure S2b. Therefore, the formation of the $SrZrO_3$ layer during the sintering process has an effect on the stability of the LSCF electrode sintered at 1000 ℃. Even though it is not the only reason for the delamination, the $SrZrO_3$ layer at least accelerates the delamination process.

In addition, the delamination phenomenon is universally observed even when a GDC interlayer is employed to prevent the interfacial reaction between LSCF and YSZ [25-27]. The mechanism proposed in this work could also provide an explanation on this phenomenon. Even if there is no formation of $SrZrO_3$ second phase for freshly prepared cell with GDC interlayer, the formation of

$SrZrO_3$ could also take place during the annealing or operation in electrolyzer mode at elevated temperature [52-54]. Post-mortem analysis after the electrolysis test also revealed the formation of the $SrZrO_3$ phase at the GDC–YSZ interface [32]. After the formation of $SrZrO_3$ second phase, delamination could proceed following the proposed mechanism. In our recent study [58], short-term (264 h) electrolysis tests were performed on half-cells with different configurations. In that work, the YSZ|GDC|LSCF cell with a thin porous GDC interlayer (1 μm), which cannot fully prevent the formation of $SrZrO_3$ second phase, also showed delamination of the LSCF electrode, inferring a relationship between the $SrZrO_3$ formation and the delamination problem. Nonetheless, the validness of the proposed mechanism will be examined on a large-area full cell with GDC interlayer fabricated by tape-casting method [59, 60]. At last, based on above proposed mechanism, to improve the stability of air electrode in SOEC, ways to prevent the formation of $SrZrO_3$ and Co-free air electrode [61] should be developed.

4. Conclusion

In this work, the mechanism for the activation and the subsequent delamination of the LSCF electrode sintered on YSZ electrolyte at 1000 ℃ in SOEC was investigated. During the electrolysis test at 1 A cm^{-2} at 800 ℃ for 24 h, R_P showed an initial activation in the first 18 h and then increased again. At the same time, R_S was relatively stable in the first 18 h followed by an abrupt increase in the last 6 hours. In addition, the initial improvement on the performance is accompanied by changes in the activation energy. The characterization of the YSZ surface after the removal of the LSCF electrode showed that a thin but dense $SrZrO_3$ layer has formed at the LSCF–YSZ interface of a freshly prepared sample. This SrZrO3 layer was proved the main contributor to the high R_P of Y1000. After the electrolysis test, it is the $SrZrO_3$ layer delaminated from the YSZ electrolyte rather than the LSCF electrode delaminated from the $SrZrO_3$ layer. EDX analysis confirmed the

diffusion of Co into the $SrZrO_3$ layer and the YSZ electrolyte. Later, the LSCF electrode with Co-containing $SrZrO_3$ layer was shown to possess better electrochemical performance and less activation effect under electrolysis current than LSCF electrode with pure $SrZrO_3$ layer. Thus, Co diffusion is most likely the reason for the activation phenomenon, which agrees with the changes in activation energy, and renders the generation of oxygen molecules at the $SrZrO_3$–YSZ interface. However, the oxygen generated cannot diffuse away efficiently due to the low porosity of the $SrZrO_3$ layer. Eventually, high oxygen partial pressure weakened the bonding and caused the delamination of the $SrZrO_3$ layer. The proposed activation and failure mechanism can also provide an explanation on the delamination phenomenon when a GDC interlayer is used. As $SrZrO_3$ may develop at some places during the long-term operation, local delamination may take place following the same process but taking longer time.

Acknowledgment

This research programme/project is funded by the National Research Foundation (NRF), Prime Minister's Office, Singapore under its Campus for Research Excellence and Technological Enterprise (CREATE) programme.

References

[1] S.M.M. Ehteshami, S.H. Chan, The role of hydrogen and fuel cells to store renewable energy in the future energy network – potentials and challenges, Energy Policy, 73 (2014) 103-109.
[2] P. Moçoteguy, A. Brisse, A review and comprehensive analysis of degradation mechanisms of solid oxide electrolysis cells, Int. J. Hydrogen Energy, 38 (2013) 15887-15902.
[3] A. Nechache, M. Cassir, A. Ringuedé, Solid oxide electrolysis cell analysis by means of electrochemical impedance spectroscopy: A review, J. Power Sources, 258 (2014) 164-181.
[4] M. Ni, M. Leung, D. Leung, Technological development of hydrogen production by solid oxide electrolyzer cell (SOEC), Int. J. Hydrogen Energy, 33 (2008) 2337-2354.
[5] M.A. Laguna-Bercero, Recent advances in high temperature electrolysis using solid oxide fuel cells: A review, J. Power Sources, 203 (2012) 4-16.
[6] J.P. Stempien, Q. Sun, S.H. Chan, Performance of power generation extension system based on solid-oxide electrolyzer cells under various design conditions, Energy, 55 (2013) 647-657.
[7] Z. Pan, Q. Liu, L. Zhang, J. Zhou, C. Zhang, S.H. Chan, Experimental and thermodynamic study on the performance of water electrolysis by solid oxide electrolyzer cells with Nb-doped Co-based perovskite anode, Applied Energy, 191 (2017) 559-567.
[8] C. Chatzichristodoulou, M. Chen, P.V. Hendriksen, T. Jacobsen, M.B. Mogensen, Understanding degradation of solid oxide electrolysis cells through modeling of electrochemical potential profiles, Electrochim. Acta, 189 (2016) 265-282.
[9] Z. Wang, M. Mori, T. Araki, Steam electrolysis performance of intermediate-temperature solid oxide electrolysis cell and efficiency of hydrogen production system at 300 Nm3 h−1, Int. J. Hydrogen Energy, 35 (2010) 4451-4458.
[10] Y. Zheng, H. Yang, Z. Pan, C. Zhang, A Ca and Fe Co-Doped Layered Perovskite as Stable Air Electrode in Solid Oxide Electrolyzer Cells under High-Current Electrolysis, Electrochim. Acta, 251 (2017) 581-587.
[11] I. Dincer, C. Acar, Review and evaluation of hydrogen production methods for better sustainability, Int. J. Hydrogen Energy, 40 (2015) 11094-11111.
[12] T. Pu, W. Tan, H. Shi, Y. Na, J. Lu, B. Zhu, Steam/CO 2 electrolysis in symmetric solid oxide electrolysis cell with barium cerate-carbonate composite electrolyte, Electrochim. Acta, 190 (2016) 193-198.
[13] J.P. Stempien, Q. Liu, M. Ni, Q. Sun, S.H. Chan, Physical principles for the calculation of equilibrium potential for co-electrolysis of steam and carbon dioxide in a Solid Oxide Electrolyzer Cell (SOEC), Electrochim. Acta, 147 (2014) 490-497.
[14] X. Yue, J.T.S. Irvine, Alternative Cathode Material for CO2 Reduction by High Temperature Solid Oxide Electrolysis Cells, J. Electrochem. Soc., 159 (2012) F442-F448.
[15] C.K. Lim, Q. Liu, J. Zhou, Q. Sun, S.H. Chan, High-temperature electrolysis of synthetic seawater using solid oxide electrolyzer cells, J. Power Sources, 342 (2017) 79-87.
[16] A.V. Virkar, Mechanism of oxygen electrode delamination in solid oxide electrolyzer cells, Int. J. Hydrogen Energy, 35 (2010) 9527-9543.
[17] K. Chen, S.P. Jiang, Failure mechanism of (La,Sr)MnO3 oxygen electrodes of solid oxide electrolysis cells, Int. J. Hydrogen Energy, 36 (2011) 10541-10549.
[18] K. Chen, N. Ai, S.P. Jiang, Performance and stability of (La,Sr)MnO3–Y2O3–ZrO2 composite oxygen electrodes under solid oxide electrolysis cell operation conditions, Int. J. Hydrogen Energy, 37 (2012) 10517-10525.

[19] S.N. Rashkeev, M.V. Glazoff, Atomic-scale mechanisms of oxygen electrode delamination in solid oxide electrolyzer cells, Int. J. Hydrogen Energy, 37 (2012) 1280-1291.
[20] J. Kim, H.-I. Ji, H.P. Dasari, D. Shin, H. Song, J.-H. Lee, B.-K. Kim, H.-J. Je, H.-W. Lee, K.J. Yoon, Degradation mechanism of electrolyte and air electrode in solid oxide electrolysis cells operating at high polarization, Int. J. Hydrogen Energy, 38 (2013) 1225-1235.
[21] M. Keane, M.K. Mahapatra, A. Verma, P. Singh, LSM–YSZ interactions and anode delamination in solid oxide electrolysis cells, Int. J. Hydrogen Energy, 37 (2012) 16776-16785.
[22] M. Laguna-Bercero, R. Campana, A. Larrea, J. Kilner, V. Orera, Electrolyte degradation in anode supported microtubular yttria stabilized zirconia-based solid oxide steam electrolysis cells at high voltages of operation, J. Power Sources, 196 (2011) 8942-8947.
[23] R. Knibbe, M.L. Traulsen, A. Hauch, S.D. Ebbesen, M. Mogensen, Solid oxide electrolysis cells: degradation at high current densities, J. Electrochem. Soc., 157 (2010) B1209-B1217.
[24] S.J. Kim, G.M. Choi, Stability of Air Electrode in Solid Oxide Electrolysis Cell, ECS Trans., 58 (2013) 139-145.
[25] H. Fan, M. Keane, P. Singh, M. Han, Electrochemical performance and stability of lanthanum strontium cobalt ferrite oxygen electrode with gadolinia doped ceria barrier layer for reversible solid oxide fuel cell, J. Power Sources, 268 (2014) 634-639.
[26] S.J. Kim, G.M. Choi, Stability of LSCF electrode with GDC interlayer in YSZ-based solid oxide electrolysis cell, Solid State Ionics, (2014).
[27] P. Hjalmarsson, X. Sun, Y.-L. Liu, M. Chen, Influence of the oxygen electrode and inter-diffusion barrier on the degradation of solid oxide electrolysis cells, J. Power Sources, 223 (2013) 349-357.
[28] J. Sar, J. Schefold, A. Brisse, E. Djurado, Durability test on coral Ce0.9Gd0.1O2-δ-La0.6Sr0.4Co0.2Fe0.8O3-δ with La0.6Sr0.4Co0.2Fe0.8O3-δ current collector working in SOFC and SOEC modes, Electrochim. Acta, 201 (2016) 57-69.
[29] Y. Zhang, K. Chen, C. Xia, S.P. Jiang, M. Ni, A model for the delamination kinetics of La0.8Sr0.2MnO3 oxygen electrodes of solid oxide electrolysis cells, Int. J. Hydrogen Energy, 37 (2012) 13914-13920.
[30] N. Li, M. Keane, M.K. Mahapatra, P. Singh, Mitigation of the delamination of LSM anode in solid oxide electrolysis cells using manganese-modified YSZ, Int. J. Hydrogen Energy, 38 (2013) 6298-6303.
[31] J. Schefold, A. Brisse, F. Tietz, Nine Thousand Hours of Operation of a Solid Oxide Cell in Steam Electrolysis Mode, J. Electrochem. Soc., 159 (2012) A137.
[32] F. Tietz, D. Sebold, A. Brisse, J. Schefold, Degradation phenomena in a solid oxide electrolysis cell after 9000 h of operation, J. Power Sources, 223 (2013) 129-135.
[33] J. Schefold, A. Brisse, H. Poepke, Long-term Steam Electrolysis with Electrolyte-Supported Solid Oxide Cells, Electrochim. Acta, (2015).
[34] Z. Pan, Q. Liu, L. Zhang, X. Zhang, S.H. Chan, Effect of Sr Surface Segregation of La0.6Sr0.4Co0.2Fe0.8O3 − δElectrode on Its Electrochemical Performance in SOC, J. Electrochem. Soc., 162 (2015) F1316-F1323.
[35] Z. Pan, Q. Liu, L. Zhang, X. Zhang, S.H. Chan, Study of Activation Effect of Anodic Current on La0.6Sr0.4Co0.2Fe0.8O3−δ Air Electrode in Solid Oxide Electrolyzer Cell, Electrochim. Acta, 209 (2016) 56-64.
[36] K. Chen, N. Li, N. Ai, Y. Cheng, W.D. Rickard, S.P. Jiang, Polarization-Induced Interface and Sr Segregation of in Situ Assembled La0.6Sr0.4Co0.2Fe0.8O3-delta Electrodes on Y2O3-

ZrO2 Electrolyte of Solid Oxide Fuel Cells, ACS applied materials & interfaces, 8 (2016) 31729-31737.
[37] H. Fan, M. Keane, N. Li, D. Tang, P. Singh, M. Han, Electrochemical stability of La0.6Sr0.4Co0.2Fe0.8O3−δ-infiltrated YSZ oxygen electrode for reversible solid oxide fuel cells, Int. J. Hydrogen Energy, 39 (2014) 14071-14078.
[38] A. Esquirol, N.P. Brandon, J.A. Kilner, M. Mogensen, Electrochemical Characterization of La[sub 0.6]Sr[sub 0.4]Co[sub 0.2]Fe[sub 0.8]O[sub 3] Cathodes for Intermediate-Temperature SOFCs, J. Electrochem. Soc., 151 (2004) A1847.
[39] W. Kong, W. Zhang, S. Zhang, Q. Zhang, S. Su, Residual stress analysis of a micro-tubular solid oxide fuel cell, Int. J. Hydrogen Energy, 41 (2016) 16173-16180.
[40] C. Fu, K. Sun, N. Zhang, X. Chen, D. Zhou, Electrochemical characteristics of LSCF–SDC composite cathode for intermediate temperature SOFC, Electrochim. Acta, 52 (2007) 4589-4594.
[41] F. Qiang, K. Sun, N. Zhang, X. Zhu, S. Le, D. Zhou, Characterization of electrical properties of GDC doped A-site deficient LSCF based composite cathode using impedance spectroscopy, J. Power Sources, 168 (2007) 338-345.
[42] J.P. Stempien, Q. Sun, S.H. Chan, Theoretical consideration of Solid Oxide Electrolyzer Cell with zirconia-based electrolyte operated under extreme polarization or with low supply of feedstock chemicals, Electrochim. Acta, 130 (2014) 718-727.
[43] S. Ji, G.Y. Cho, W. Yu, P.C. Su, M.H. Lee, S.W. Cha, Plasma-enhanced atomic layer deposition of nanoscale yttria-stabilized zirconia electrolyte for solid oxide fuel cells with porous substrate, ACS applied materials & interfaces, 7 (2015) 2998-3002.
[44] S. Ha, P.-C. Su, S.-W. Cha, Combinatorial deposition of a dense nano-thin film YSZ electrolyte for low temperature solid oxide fuel cells, Journal of Materials Chemistry A, 1 (2013) 9645.
[45] Q. Liu, K.A. Khor, S.H. Chan, X.J. Chen, Anode-supported solid oxide fuel cell with yttria-stabilized zirconia/gadolinia-doped ceria bilayer electrolyte prepared by wet ceramic co-sintering process, J. Power Sources, 162 (2006) 1036-1042.
[46] K. Chen, N. Li, N. Ai, M. Li, Y. Cheng, W.D.A. Rickard, J. Li, S.P. Jiang, Direct application of cobaltite-based perovskite cathodes on the yttria-stabilized zirconia electrolyte for intermediate temperature solid oxide fuel cells, J. Mater. Chem. A, 4 (2016) 17678-17685.
[47] H. Schichlein, A.C. Müller, M. Voigts, A. Krügel, E. Ivers-Tiffée, Deconvolution of electrochemical impedance spectra for the identification of electrode reaction mechanisms in solid oxide fuel cells, J. Appl. Electrochem., 32 (2002) 875-882.
[48] A. Leonide, V. Sonn, A. Weber, E. Ivers-Tiffée, Evaluation and Modeling of the Cell Resistance in Anode-Supported Solid Oxide Fuel Cells, J. Electrochem. Soc., 155 (2008) B36.
[49] K. Kammer Hansen, M. Menon, J. Knudsen, N. Bonanos, M. Mogensen, The Effect of a CGO Barrier Layer on the Performance of LSM/YSZ SOFC Cathodes, J. Electrochem. Soc., 157 (2010) B309.
[50] K. Hansen, K. Hansen, A-site deficient (La0.6Sr0.4)1−sFe0.8Co0.2O3−δ perovskites as SOFC cathodes, Solid State Ionics, 178 (2007) 1379-1384.
[51] S.P. Jiang, W. Wang, Effect of Polarization on the Interface Between (La,Sr)MnO[sub 3] Electrode and Y[sub 2]O[sub 3]-ZrO[sub 2] Electrolyte, Electrochem. Solid-State Lett., 8 (2005) A115.
[52] F. Wang, M.E. Brito, K. Yamaji, D.-H. Cho, M. Nishi, H. Kishimoto, T. Horita, H. Yokokawa, Effect of polarization on Sr and Zr diffusion behavior in LSCF/GDC/YSZ system, Solid State Ionics, 262 (2014) 454-459.

[53] F. Wang, M. Nishi, M.E. Brito, H. Kishimoto, K. Yamaji, H. Yokokawa, T. Horita, Sr and Zr diffusion in LSCF/10GDC/8YSZ triplets for solid oxide fuel cells (SOFCs), J. Power Sources, 258 (2014) 281-289.
[54] J. Laurencin, M. Hubert, D.F. Sanchez, S. Pylypko, M. Morales, A. Morata, B. Morel, D. Montinaro, F. Lefebvre-Joud, E. Siebert, Degradation mechanism of La 0.6 Sr 0.4 Co 0.2 Fe 0.8 O 3-δ /Gd 0.1 Ce 0.9 O 2-δ composite electrode operated under solid oxide electrolysis and fuel cell conditions, Electrochim. Acta, 241 (2017) 459-476.
[55] W. Jung, H.L. Tuller, Investigation of surface Sr segregation in model thin film solid oxidefuel cell perovskite electrodes, Energy Environ. Sci., 5 (2012) 5370-5378.
[56] W. Lee, J.W. Han, Y. Chen, Z. Cai, B. Yildiz, Cation size mismatch and charge interactions drive dopant segregation at the surfaces of manganite perovskites, J Am Chem Soc, 135 (2013) 7909-7925.
[57] P.-n. Huang, A. Petric, Electrical conduction of yttrium-doped strontium zirconate, Journal of Materials Chemistry, 5 (1995) 53-56.
[58] Z. Pan, Q. Liu, R. Lyu, P. Li, S.H. Chan, Effect of La0.6Sr0.4Co0.2Fe0.8O3−δ air electrode–electrolyte interface on the short-term stability under high-current electrolysis in solid oxide electrolyzer cells, J. Power Sources, 378 (2018) 571-578.
[59] J. Zhou, Q. Liu, L. Zhang, Z. Pan, S.H. Chan, Influence of pore former on electrochemical performance of fuel-electrode supported SOFCs manufactured by aqueous-based tape-casting, Energy, 115 (2016) 149-154.
[60] J. Zhou, Q. Liu, L. Zhang, S.H. Chan, A study of short stack with large area solid oxide fuel cells by aqueous tape casting, Int. J. Hydrogen Energy, 41 (2016) 18203-18206.
[61] F. Dong, Y. Chen, D. Chen, Z. Shao, Surprisingly high activity for oxygen reduction reaction of selected oxides lacking long oxygen-ion diffusion paths at intermediate temperatures: a case study of cobalt-free BaFeO(3-delta), ACS applied materials & interfaces, 6 (2014) 11180-11189.

Tables

Table 1. Results of EDX examinations of the electrolyte surfaces of Y1000 (half-cells with LSCF electrode sintered at 1000 ℃), including freshly-prepared sample and samples after electrolysis test for different periods (0.5 h, 12 h and 24 h) under 1 A cm^{-2} at 800 ℃

		La	Sr	Co	Fe	Zr	O
Freshly-prepared Sample (at. %)[1]		4	12			25	58
After 0.5 h Electrolysis test (at. %)[1]	C1[3]	3	12	14	3	16	52
	C2	4	17	6	2	21	50
	C3	5	17	9	2	20	47
	C4	3	14	6	2	17	58
	C Average	4	15	8	2	19	52
	D	2	13	2	4	17	62
After 12 h Electrolysis test (at. %)[2]	E1			11		23	66
	E2			9		28	63
	E3			13		22	65
	E4			7		26	67
	F1			2		37	61
	F2			3		29	68
	F3			3		38	59
	F4			3		31	66
	E Average			10		25	65
	F Average			3		34	63
	G			5		28	67
After 24 h Electrolysis test (at. %)[2]	A	4	16	3		20	57
	B			5		30	65

1: The LSCF electrodes of these two samples were removed by ultrasound treatment in diluted nitric acid for 30 min.

2: The electrolyte surfaces of these two samples were observed directly as LSCF electrodes has partially or completely delaminated from the electrolyte.

3: Capital letters indicate the places where the EDX examinations were performed, which are also indicated in Figure 3b, 5b, 5c, 6b and 6c. C, E and F are point-scans while A, B, D and G are area-scans.

Figure Captions

Figure 1. (a) Evolution of Nyquist plot extracted under OCV, (b) evolution of resistances and voltage and (c) DRT analysis of Y1000 (half-cell with LSCF electrode sintered at 1000 ℃); (d) Evolution of Nyquist plot extracted under OCV, (e) evolution of resistances and voltage and (f) DRT analysis of Y800 (half-cell with LSCF electrode sintered at 800 ℃). (Electrolysis test was conducted with a current of 1 A cm^{-2} at 800 ℃ for 24 h. In (c) and (f), H, M and L denote high-, medium- and low-frequency process and L' denotes additional low-frequency process of Y800)

Figure 2. Evolution of medium-frequency arc, low-frequency arc and total activation energy during the first 2 h of the electrolysis test under 1 A cm^{-2} at 800 ℃ for Y1000 (half-cell with LSCF electrode sintered at 1000 ℃)

Figure 3. FESEM images and EDX results of Y1000 (half-cells with LSCF electrode sintered at 1000 ℃) and Y800 (half-cells with LSCF electrode sintered at 800 ℃) before the test. (a) Cross-section of Y1000; (b) surface of YSZ electrolyte of Y1000 after the removal of the LSCF electrode; (c) surface of YSZ electrolyte of Y800 after the removal of the LSCF electrode; (d) A bare YSZ electrolyte surface. The yellow rectangle indicates the area of EDX examination.

Figure 4. XRD patterns of the YSZ surface after the removal of the LSCF electrode. (a) Y1000 (half-cells with LSCF electrode sintered at 1000 ℃) before the electrolysis test; (b) Y800 (half-cells with LSCF electrode sintered at 800 ℃) before the electrolysis test; (c) Y1000 after the electrolysis test.

Figure 5. (a) An overview FESEM image of the YSZ electrolyte surface of Y1000 (half-cells with LSCF electrode sintered at 1000 ℃) after the electrolysis test under 1 A cm^{-2} for 24 h at 800 ℃;

(b) An enlarged image of point A in Figure 5a; (c) An enlarged image of point B in Figure 5a. The yellow rectangles indicate the area of EDX examination.

Figure 6. FESEM images of the surfaces of the YSZ electrolytes of Y1000 (half-cells with LSCF electrode sintered at 1000 ℃) (a) before and (b-d) after the electrolysis test under 1 A cm^{-2} at 800 ℃ for different periods: (b) 0.5 h, (c) 12 h and (d) 24 h.

Figure 7. Changes of R_P along testing temperature for (a) Y1000 and (b) re-applied LSCF electrode sintering at 800 ℃ after the removal of LSCF electrode of Y1000

Figure 8. (a) SEM image of the YSZ electrolyte surface after the removal of the re-applied LSCF electrode sintered at 1000 ℃ by acid washing (XRD pattern and EDX analysis of the surface are shown in the insets); (b) Evolution of R_P for newly prepared Y1000 during the 24 h electrolysis test with an anodic current of 1 A cm^{-2} at 800 ℃ and evolution of R_P for the re-applied LSCF electrode sintered at 1000 ℃ for another electrolysis test under the same condition

Figure 9. Schematic of the mechanism for the activation and delamination of LSCF air electrode of Y1000 (half-cells with LSCF electrode sintered at 1000 ℃). (a) Freshly prepared sample; (b) Sample after 0.5 h high-current electrolysis; (c) Sample during the high-current electrolysis test; (d) Sample after 12 h electrolysis test; (e) Sample after 24 h electrolysis test.

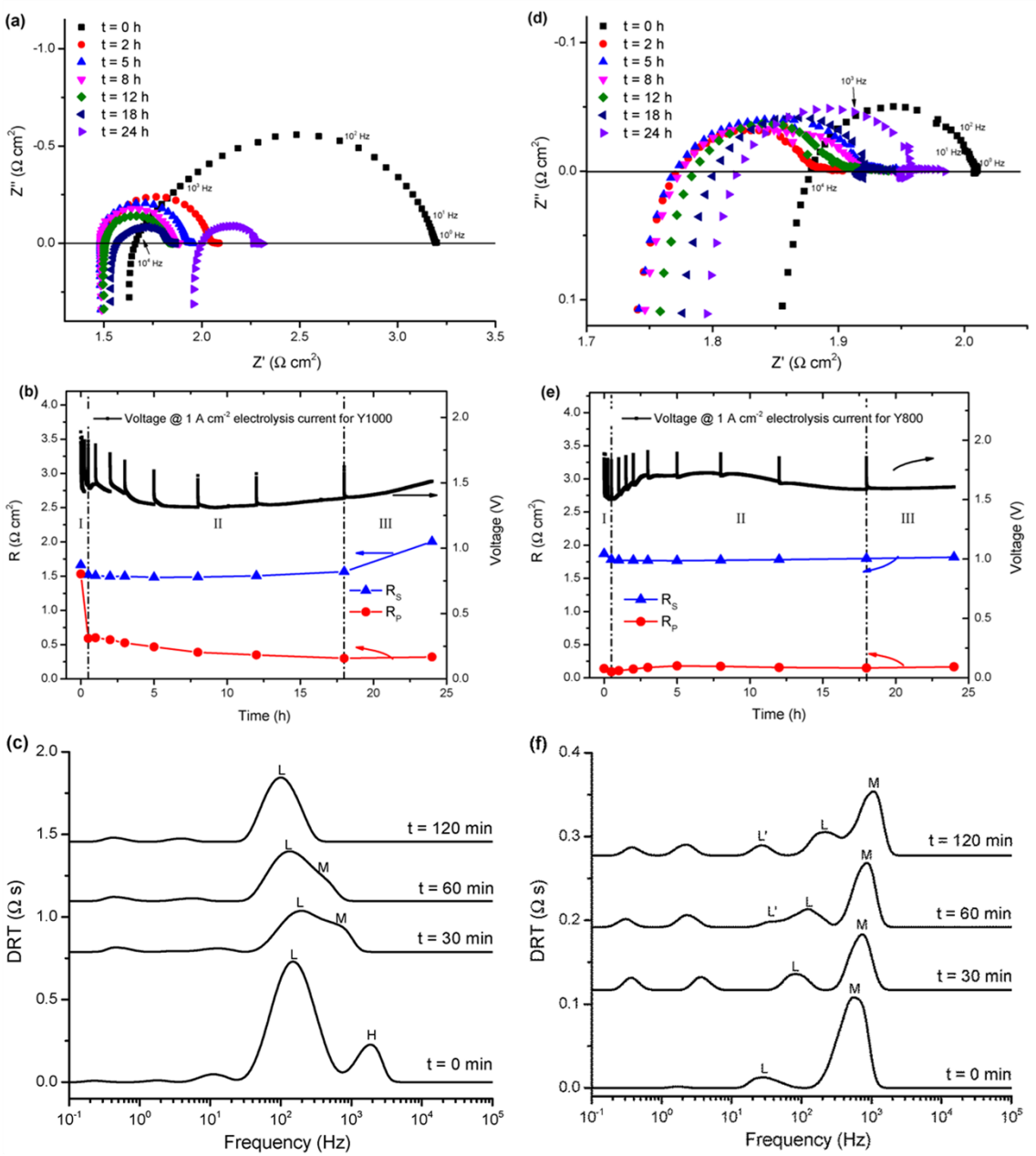

Figure 1. (a) Evolution of Nyquist plot extracted under OCV, (b) evolution of resistances and voltage and (c) DRT analysis of Y1000 (half-cell with LSCF electrode sintered at 1000 ℃); (d) Evolution of Nyquist plot extracted under OCV, (e) evolution of resistances and voltage and (f) DRT analysis of Y800 (half-cell with LSCF electrode sintered at 800 ℃). (Electrolysis test was conducted with a current of 1 A cm^{-2} at 800 ℃ for 24 h. In (c) and (f), H, M and L denote high-, medium- and low-frequency process and L' denotes additional low-frequency process of Y800)

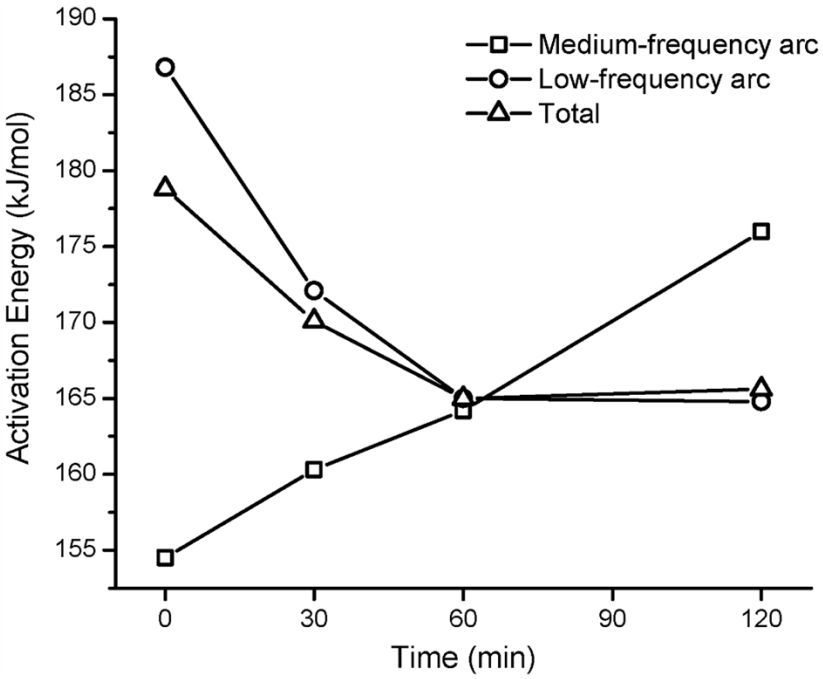

Figure 2. Evolution of medium-frequency arc, low-frequency arc and total activation energy during the first 2 h of the electrolysis test under 1 A cm^{-2} at 800 ℃ for Y1000 (half-cell with LSCF electrode sintered at 1000 ℃)

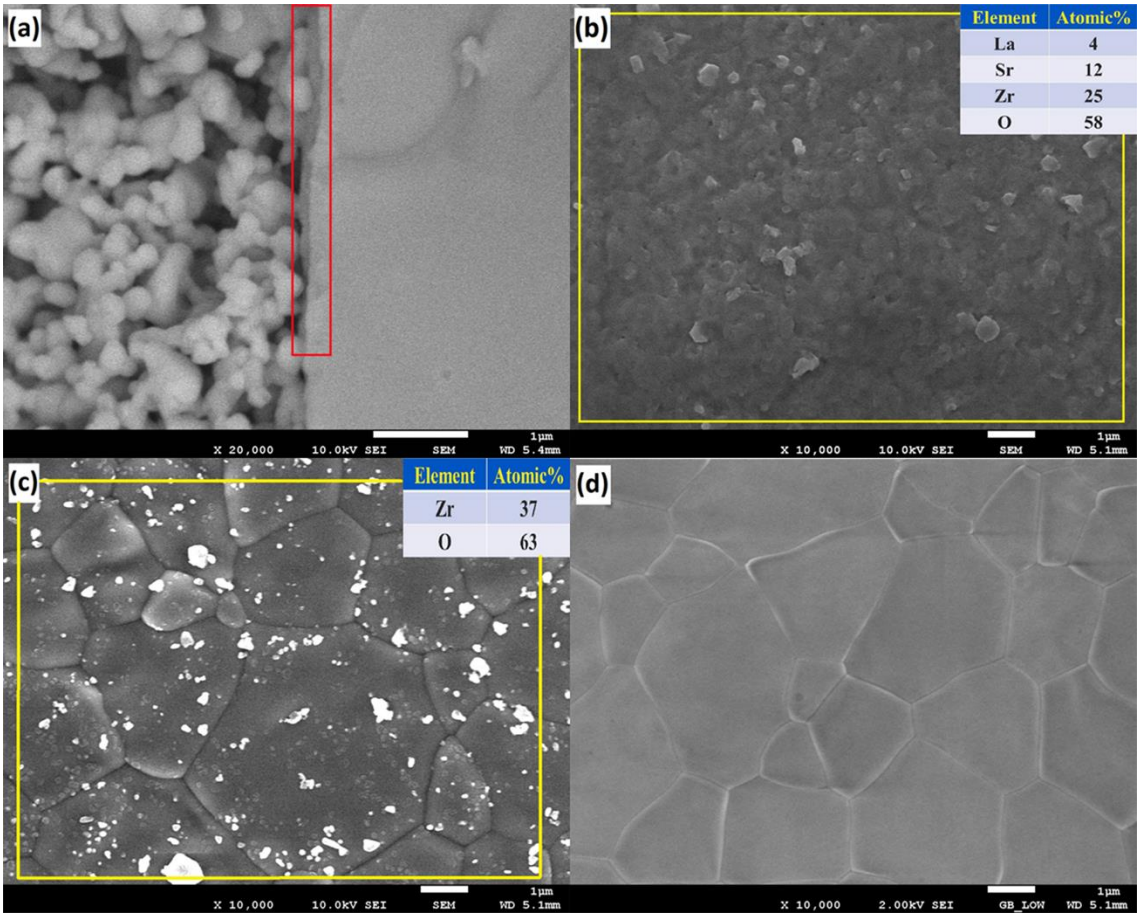

Figure 3. FESEM images and EDX results of Y1000 (half-cells with LSCF electrode sintered at 1000 ℃) and Y800 (half-cells with LSCF electrode sintered at 800 ℃) before the test. (a) Cross-section of Y1000; (b) surface of YSZ electrolyte of Y1000 after the removal of the LSCF electrode; (c) surface of YSZ electrolyte of Y800 after the removal of the LSCF electrode; (d) A bare YSZ electrolyte surface. The yellow rectangle indicates the area of EDX examination.

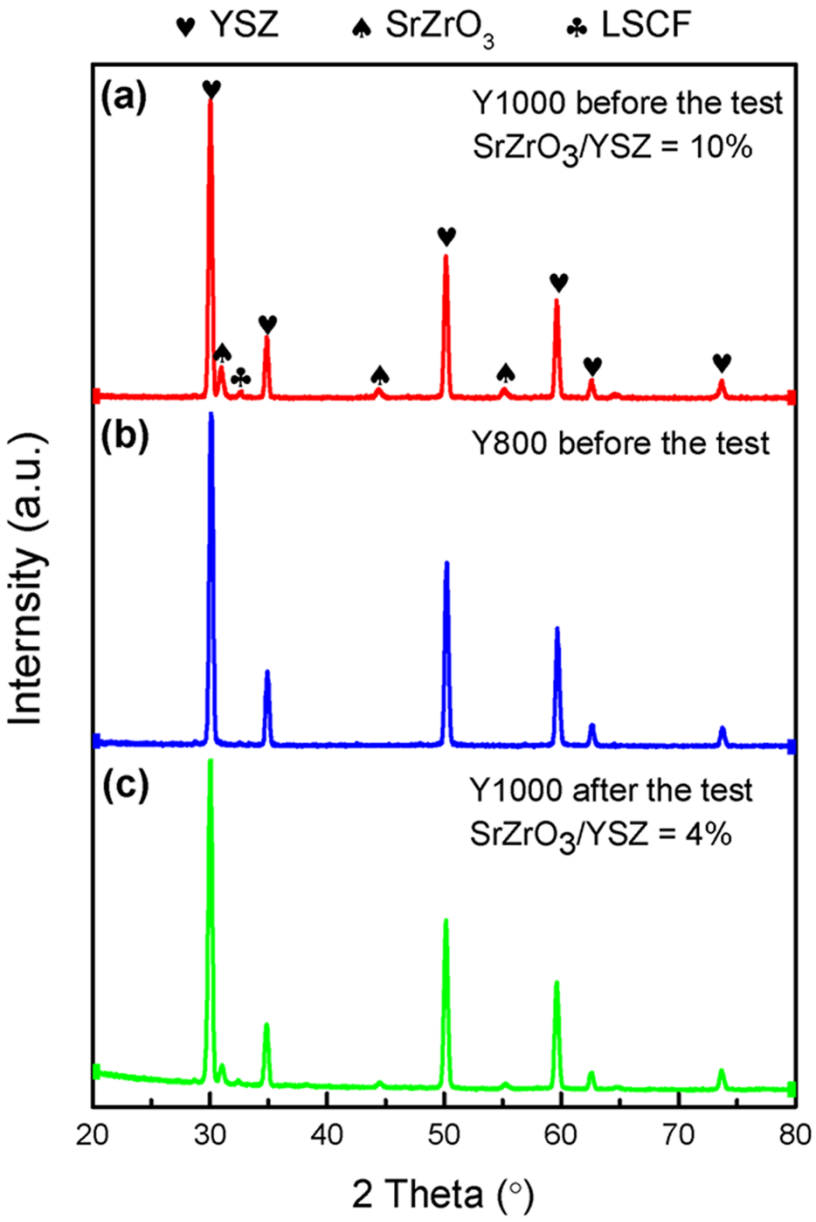

Figure 4. XRD patterns of the YSZ surface after the removal of the LSCF electrode. (a) Y1000 (half-cells with LSCF electrode sintered at 1000 ℃) before the electrolysis test; (b) Y800 (half-cells with LSCF electrode sintered at 800 ℃) before the electrolysis test; (c) Y1000 after the electrolysis test.

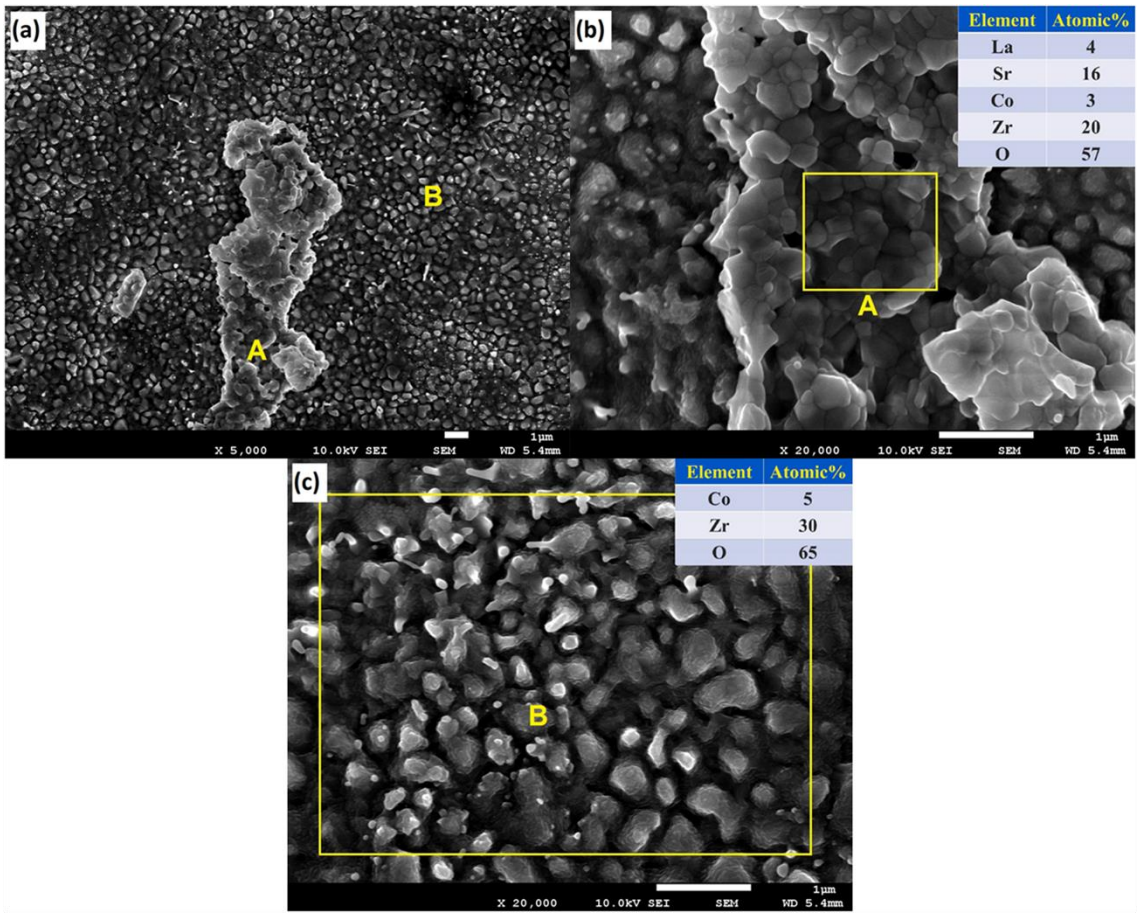

Figure 5. (a) An overview FESEM image of the YSZ electrolyte surface of Y1000 (half-cells with LSCF electrode sintered at 1000 ℃) after the electrolysis test under 1 A cm^{-2} for 24 h at 800 ℃; (b) An enlarged image of point A in Figure 5a; (c) An enlarged image of point B in Figure 5a. The yellow rectangles indicate the area of EDX examination.

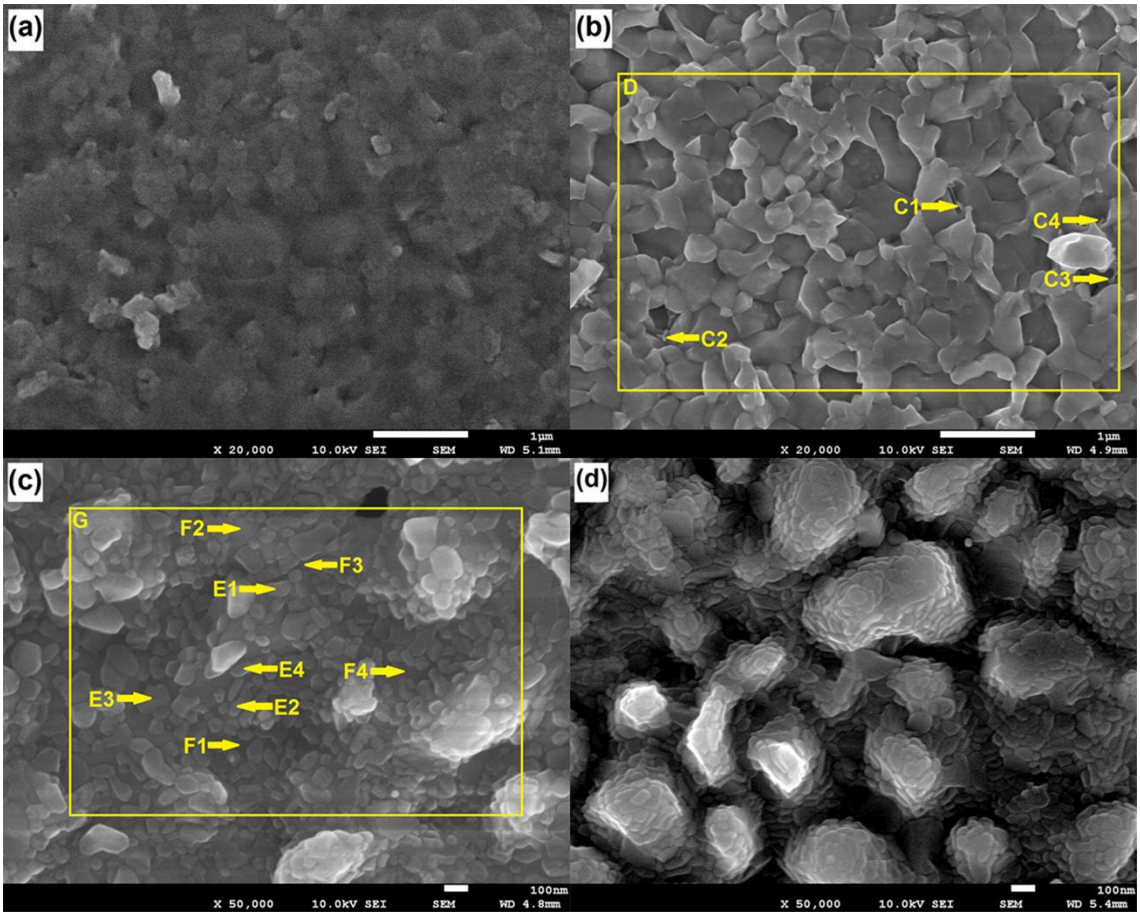

Figure 6. FESEM images of the surfaces of the YSZ electrolytes of Y1000 (half-cells with LSCF electrode sintered at 1000 ℃) (a) before and (b-d) after the electrolysis test under 1 A cm^{-2} at 800 ℃ for different periods: (b) 0.5 h, (c) 12 h and (d) 24 h.

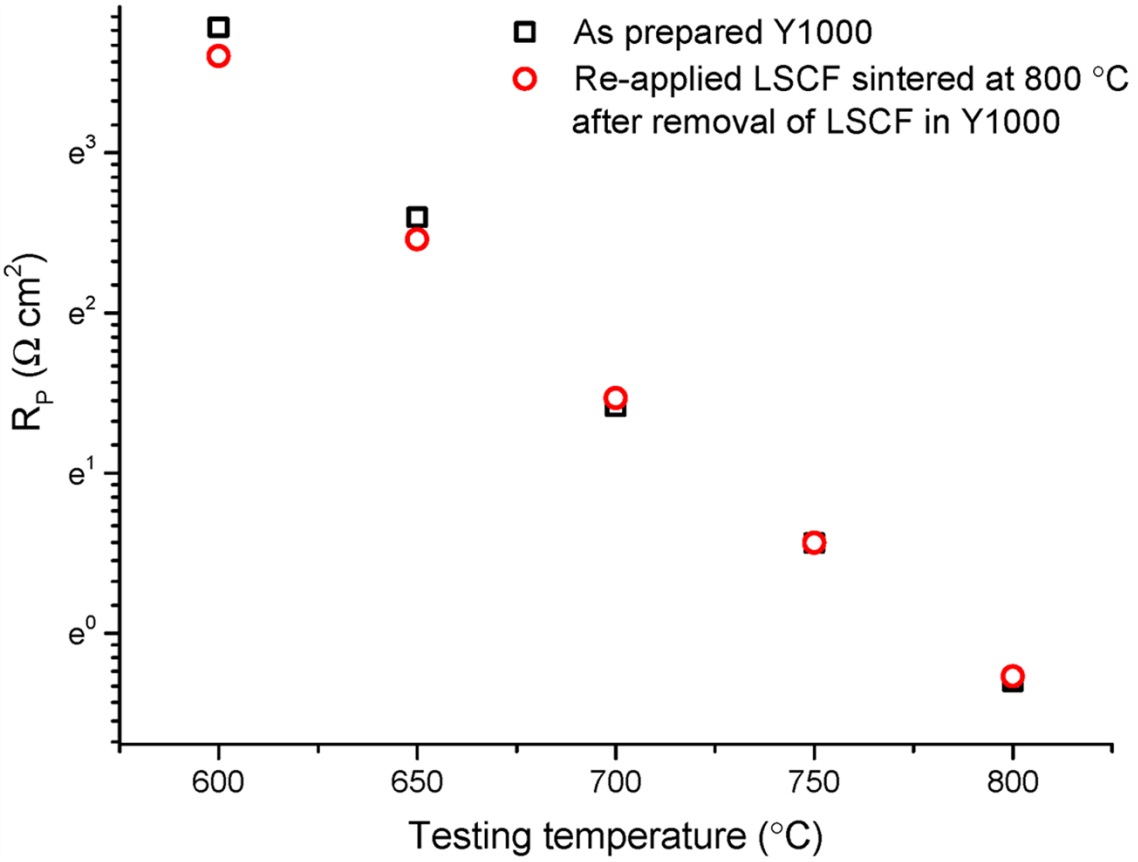

Figure 7. Changes of R_P along testing temperature for (a) Y1000 and (b) re-applied LSCF electrode sintering at 800 ℃ after the removal of LSCF electrode of Y1000

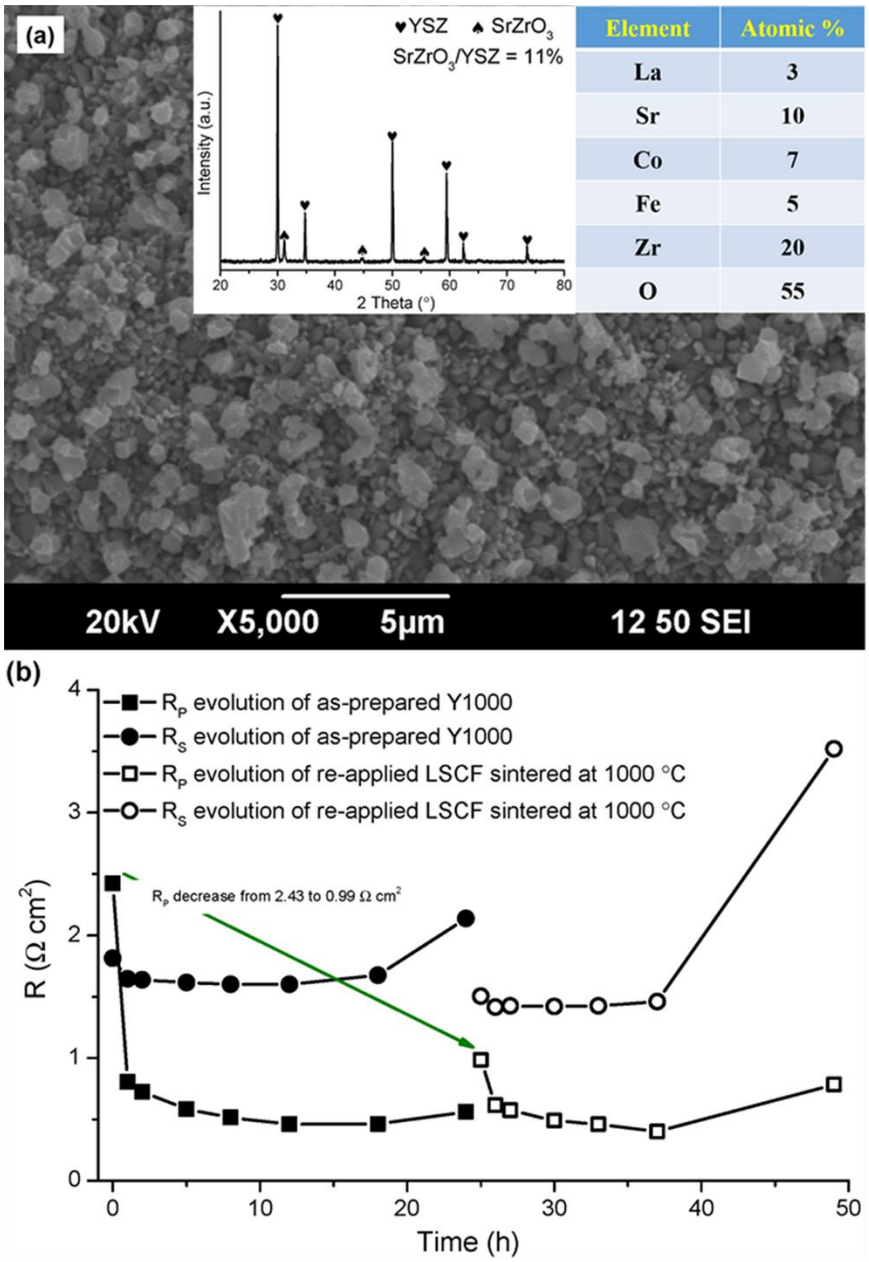

Figure 8. (a) SEM image of the YSZ electrolyte surface after the removal of the re-applied LSCF electrode sintered at 1000 ℃ by acid washing (XRD pattern and EDX analysis of the surface are shown in the insets); (b) Evolution of R_P for newly prepared Y1000 during the 24 h electrolysis test with an anodic current of 1 A cm^{-2} at 800 ℃ and evolution of R_P for the re-applied LSCF electrode sintered at 1000 ℃ for another electrolysis test under the same condition

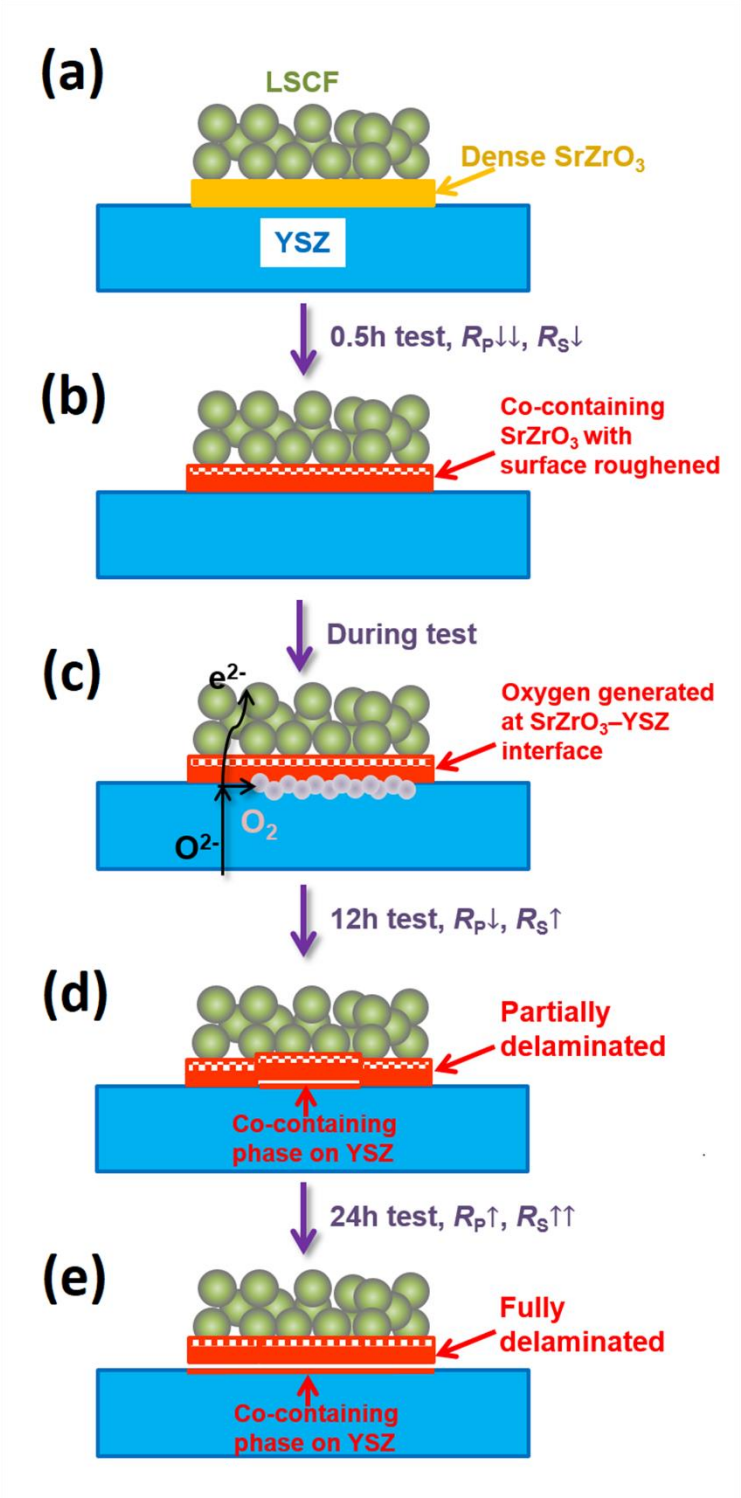

Figure 9. Schematic of the mechanism for the activation and delamination of LSCF air electrode of Y1000 (half-cells with LSCF electrode sintered at 1000 ℃). (a) Freshly prepared sample; (b) Sample after 0.5 h high-current electrolysis; (c) Sample during the high-current electrolysis test; (d) Sample after 12 h electrolysis test; (e) Sample after 24 h electrolysis test.